

ULRR

Geometry effects on interfacial dynamics of gas#driven drainage in a gradient capillary

Item Type	Article
Authors	Suo, Si;O'Kiely, Doireann;Liu, Mingchao;Gan, Yixiang
Citation	Water Resources Research, 60, e2023WR036766.
Publisher	American Geophysical Union
Download date	2026-04-17 22:33:58
Item License	https://creativecommons.org/licenses/by-nc-sa/4.0/
Link to Item	https://doi.org/10.34961/researchrepository-ul.27003619

Water Resources Research®

RESEARCH ARTICLE

10.1029/2023WR036766

Geometry Effects on Interfacial Dynamics of Gas-Driven Drainage in a Gradient Capillary



Key Points:

- We numerically investigate the dynamics of a gas-liquid interface during drainage in a gradient capillary tube
- The observations from our numerical simulations can be rationalized by an adapted theoretical model
- We find a unique stabilization in drainage along expanding tubes, suppressing film entrainment even when the system is initially unstable

Si Suo¹ , Doireann O'Kiely² , Mingchao Liu³, and Yixiang Gan⁴ 

¹Department of Engineering Mechanics, Linné Flow Centre, KTH Royal Institute of Technology, Stockholm, Sweden, ²Department of Mathematics and Statistics, MACSI, University of Limerick, Limerick, Ireland, ³Department of Mechanical Engineering, University of Birmingham, Birmingham, UK, ⁴School of Civil Engineering, The University of Sydney, Sydney, NSW, Australia

Correspondence to:

S. Suo,
ssu@kth.se

Citation:

Suo, S., O'Kiely, D., Liu, M., & Gan, Y. (2024). Geometry effects on interfacial dynamics of gas-driven drainage in a gradient capillary. *Water Resources Research*, 60, e2023WR036766. <https://doi.org/10.1029/2023WR036766>

Received 21 NOV 2023

Accepted 8 JUL 2024

Abstract Unfavorable fluid-fluid displacement, where a low-viscosity fluid displaces a higher-viscosity fluid in permeable media, is commonly encountered in various subsurface processes. Understanding the formation and evolution of the resulting interfacial instability can have practical benefits for engineering applications. Using gradient capillary tubes as surrogate models of permeable media, we numerically investigate interfacial dynamics during gas-driven drainage. Our focus is on understanding the impact of tube geometry on interface stability. In a gradient tube, since the interface shape changes during the drainage process, we measure interfacial stability using the difference between the contact-line velocity U_{cl} and the meniscus tip velocity U_{tip} . We define instability as a rapid reduction in the contact line velocity U_{cl} compared to the tip velocity U_{tip} . Beyond the onset of this instability, gas penetrates into the liquid, forming a finger, and entraining a liquid film on the tube wall. The observed stability transition can be rationalized to a large extent by adaptation of an existing theory for cylindrical tubes in terms of a critical capillary number Ca_{crit} . For an expanding tube, simulations suggest that a stability transition from an initially unstable meniscus to a final stable one, with U_{cl} catching up with U_{tip} , can occur if the local capillary number is initially slightly larger than Ca_{crit} and then drops below Ca_{crit} . The insights gained from this study can be beneficial in estimating the mode and efficiency of subsurface fluid displacement.

1. Introduction

Immiscible fluid-fluid displacements in confined geometries play an essential role in various subsurface engineering processes, such as carbon geological sequestration (Cuéllar-Franca & Azapagic, 2015), underground hydrogen storage (Muhammed et al., 2022), enhanced oil recovery (Khishvand et al., 2017), and nonaqueous phase liquid (NAPL) remediation (Yuan et al., 2021). Accurate understanding of the underlying pore-scale dynamics, particularly the interfacial stability, is essential for capturing the flow patterns in these applications. Interfacial instabilities, commonly referred to as fingering phenomena, often hinder engineering practices and limit their efficiency (Li et al., 2019; Yang et al., 2019). Thus, knowledge of the formation and evolution of the fingers is crucial for these processes.

The dynamics of immiscible two-phase flow are governed by the competition between viscous and capillary forces. As a result, flow patterns can be primarily characterized by the capillary number Ca and the viscosity ratio M of the defending phase over the invading phase. When a fluid of low viscosity displaces a fluid of higher viscosity, that is, unfavorable displacement ($M > 1$), in a confined space, the interface may become unstable and viscous fingers can dominate the flow pattern, as shown in the seminal work of Saffman and Taylor (1958). The stability problem becomes more complex when fluid-solid interaction is involved. Early experimental studies (Levaché & Bartolo, 2014; Setu et al., 2013) have revealed that the presence of moving contact lines results in a diverse range of patterns within the forced imbibition regime. In the drainage regime (a non-wetting phase displacing a wetting phase), recent microfluidic experiments in capillaries (Pahlavan et al., 2019; Zhao et al., 2018) have demonstrated that gas-driven drainage can lead to the entrainment of liquid films and eventual formation of Taylor bubbles (Taylor, 1961) when the capillary number exceeds a critical value. Gao et al. (2019) further developed a theoretical prediction for the critical capillary number Ca_{crit} at which the apparent contact angle vanishes and entrainment begins,

$$Ca_{crit} = \frac{\theta_{eq}^3}{9} \left[\ln \left(\frac{Ca_{crit}^{1/3} \theta_{eq}}{18^{1/3} \pi Ai^2 (s_{max}) \lambda} \right) \right]^{-1}, \quad (1)$$

© 2024. The Author(s).

This is an open access article under the terms of the [Creative Commons Attribution-NonCommercial-NoDerivs License](https://creativecommons.org/licenses/by/4.0/), which permits use and distribution in any medium, provided the original work is properly cited, the use is non-commercial and no modifications or adaptations are made.

where θ_{eq} is the equilibrium contact angle, Ai is an Airy function with $s_{max} = -1.01879\dots$ is defined by $Ai'(s_{max}) = 0$, and λ is the dimensionless slip length. We note that the critical capillary number is strongly dependent on the equilibrium contact angle. At a larger scale, interfacial instability emerges as a fractal pattern during the unfavorable displacement in permeable media (Chen et al., 2017; Holtzman & Segre, 2015; Zhao et al., 2016). In addition to the viscous fingering that occurs at larger values of Ca and M , another instability pattern, that is, capillary fingering, dominated by capillary effects, can form in the low- Ca regime. The transition between these two patterns has been extensively studied and can be summarized using Lenormand's phase diagram, which takes into account the parameters of Ca , M , and θ_{eq} (Primkulov et al., 2021).

In addition to the three dimensionless parameters mentioned above, recent studies have increasingly suggested that pore-scale geometries have a significant impact on interfacial dynamics. Chen et al. (2017) conducted experimental studies on immiscible displacement in rough fractures and observed film entrainment along with a reduction in displacement efficiency, which shares similarities with phenomena reported in Levaché and Bartolo (2014), but with a particular emphasis on the contribution of surface roughness. Furthermore, the use of specific geometric designs to control interfacial instabilities has shown promising potential. For instance, Hele-Shaw experiments on air-oil drainage performed by Al-Housseiny et al. (2012) demonstrated that a gradient in flow passage could fundamentally control interfacial dynamics. It has also been found that a pore size gradient in porous media can help suppress fingerings (Lu et al., 2019; Rabbani et al., 2018; Vincent-Dospital et al., 2022). Moreover, Suo et al. comprehensively investigated the two-phase flow in hierarchical porous media and suggested that well-designed two-order pore spaces help suppress viscous fingering (Suo et al., 2020) and capillary fingering (Suo & Gan, 2021). However, the quantitative dependence of flow instabilities on geometry and the underlying interfacial dynamics are not well established.

In this work, we aim to investigate the impacts of geometry on interfacial dynamics during gas-driven drainage using numerical simulations and lubrication theory. The capillary tube, as a widely used surrogate, is employed for investigating the fundamental physics and dynamics involved in flows within porous media. The rest of this work is structured as follows. In Section 2, a numerical model was built up based on the phase-field method for simulating the drainage process in contracting and expanding capillary tubes, and the corresponding controlling parameters and the stability condition were clarified. In Section 3, the impacts of the tube geometry on interfacial dynamics and stability were demonstrated through numerical results. We then developed a theoretical solution of critical capillary number, similar to Equation 1, to rationalize the observations from numerical simulations. In Section 4, we investigate post-instability dynamics including interfacial pinch-off. Finally, we present our conclusions in Section 5.

2. Numerical Modeling

2.1. Governing Equations and Boundary Conditions

We use the phase-field (PF) method (Jacqmin, 1999; Yue et al., 2004) to simulate the drainage process. Assuming the drainage flow inside a capillary tube is very slow (Reynolds number $Re \ll 1$), the pressure p , velocity \mathbf{v} and phase-field variable ϕ can be described by Stokes equations coupled with the Cahn-Hilliard equations.

$$\nabla \cdot \mathbf{v} = 0, \quad (2)$$

$$\partial\phi/\partial t + \mathbf{v} \cdot \nabla\phi = \gamma\nabla^2 G, \quad (3)$$

$$-\nabla p + \mu(\phi)\nabla^2\mathbf{v} + G\nabla\phi = 0. \quad (4)$$

Equation 2 is a conservation-of-mass rule. Equation 3 describes the two-phase nature of the flow: $\phi \in [-1, 1]$ defines the liquid ($\phi = 1$) and the gas ($\phi = -1$) phases and thus the interface position ($\phi = 0$). On the right-hand-side, γ is the mobility and G is the bulk chemical potential, given by

$$G = \omega[-\nabla^2\phi + (\phi^2 - 1)\phi/\epsilon^2], \quad (5)$$

where ϵ is the interface thickness and ω is the mixing energy density which is related to the surface tension $\sigma = 2\sqrt{2}\omega/(3\epsilon)$. Finally, Equation 4 is a conservation-of-momentum law, where we assume the viscosity of

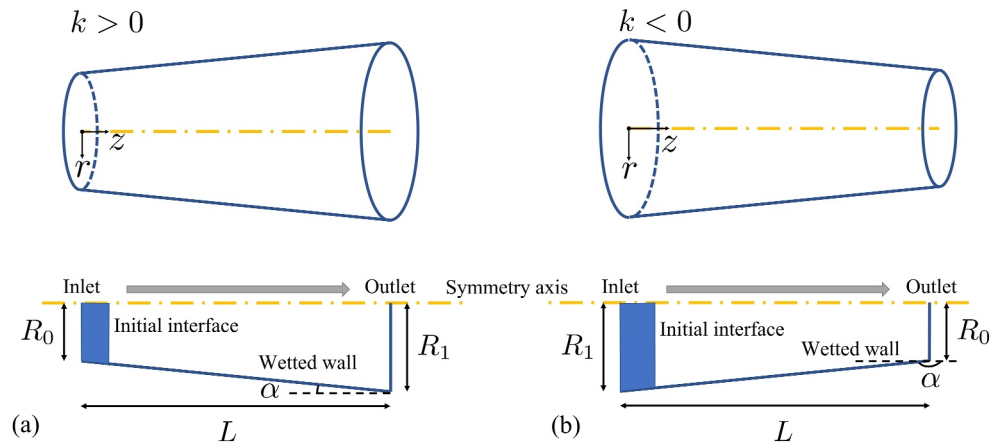


Figure 1. Schematic of numerical models for drainage: a wetting liquid is displaced by a non-wetting gas in (a) an expanding capillary tube and (b) a contracting capillary tube.

mixed fluids takes the arithmetic mean value, that is, $\mu(\phi) = \frac{1+\phi}{2}\mu_l + \frac{1-\phi}{2}\mu_g$ (which recovers the viscosity of liquid phase μ_l and gas phase μ_g away from the interface), and the term $G\nabla\phi$ represents interfacial forces.

We apply our phase-field model to drainage in gradient capillary tubes, as illustrated in Figure 1. Assuming the flow is axisymmetric, we define cylindrical polar coordinates with z pointing along the length of the tube and r pointing in the radial direction, and solve in the rz plane. The tube gradient k is defined by $k = (R_{in} - R_{out})/L$, where L is the tube length and R_{in} and R_{out} are the tube radius at the inlet and outlet respectively, and the slope angle $\alpha = \arctan k$, correspondingly. We set the smaller radius $\min(R_{in}, R_{out}) = R_0$ and the larger one $\max(R_{in}, R_{out}) = R_1$, and fix $R_1 = 2R_0$ and $L = 20R_0$, resulting in two geometric settings: an expanding tube ($k = 0.05$) and a contracting tube ($k = -0.05$). We consider a model problem of displacement of a liquid phase from a capillary tube by injection of a gas phase at a fixed inlet flow rate Q_{in} , with the outlet connected to the ambient environment. Initially, the interface is flat and located $0.5R_0$ away from the inlet. To simulate the contact line moving along the wetted wall, besides the no-slip condition, boundary conditions for ϕ are.

$$\mathbf{n}_w \cdot \nabla G = 0, \quad (6)$$

$$\omega \mathbf{n}_w \cdot \nabla \phi = (3/4)\sigma(1 - \phi^2) \cos \theta_{eq}, \quad (7)$$

Where \mathbf{n}_w is the wall normal vector and θ_{eq} is the equilibrium contact angle measured within the liquid phase. This implementation of wall wettability can guarantee the consistency of the ϕ profile around the contact line on the wall and across the interface within the bulk (Jacqmin, 2000).

2.2. Numerical Implementation

The model outlined in Section 2.1 is solved numerically using the finite element method via COMSOL Multiphysics®. We used triangular elements to mesh the trapezoidal domain, with mixed-order shape functions, that is, second-order (quadratic) for velocities and linear for other variables. The appropriate time step is determined by the Courant–Friedrichs–Lewy (CFL) number, and we set its upper limit to 0.5 to ensure numerical convergence. The numerical scheme has been validated by comparing against a theoretical solution for a uniform tube, see Appendix A.

2.3. Controlling Parameters

In our numerical simulations, we solve a non-dimensionalized version of Equations 2–7. All lengths are scaled by R_0 , and all times are scaled by $\pi LR_0^2/Q_{in}$. The dimensionless problem is governed by the slope angle α , the wettability θ_{eq} , Cahn number Cn , relative slip length S , viscosity ratio M and capillary number Ca , which are introduced and defined below.

2.3.1. Slip Length and Interface Thickness

Macroscopic lengths arising in the Cahn-Hilliard model have a strong influence on capillary-dominated flows. In particular, the bulk chemical potential G depends on an assumed interface thickness ϵ and diffuses across the interface over a diffusion lengthscale $l_d = \sqrt{\gamma\mu_{\text{eff}}}$ (Yue et al., 2010), where $\mu_{\text{eff}} = \sqrt{\mu_g\mu_l}$ and γ is an artificial parameter which plays the role of a diffusion coefficient. To make an appropriate choice of γ and l_d , one can usually introduce the notion of a slip length l_s , which emerges from the microscopic physical origins of contact line motion and leads to a rational solution of macroscopic hydrodynamics far from the contact lines (Cox, 1986; Eggers, 2005). The connection of l_d to l_s was first suggested in (Jacqmin, 2000), and numerical data suggests the choice $l_s = 2.5l_d$ (Yue & Feng, 2011). Then, this equation was further validated by the comparison between the simulation and an asymptotic solution in the situation of dewetting in a capillary tube (Gao et al., 2019).

The choice of interface thickness ϵ is driven by a balance between model accuracy and computational efficiency. Smaller values of ϵ are closer to the reality of a nanoscale interface, and yield less energy dissipation. However, reducing ϵ requires finer meshing of the computational domain and hence increases computational time. To compromise, ϵ , characterized by the Cahn number $\text{Cn} = \epsilon/R_0$, should be selected by the requirement of just attaining the sharp-interface limit, below which the numerical results no longer depend on the Cn . Previous resolution sensitivity studies suggested that $\text{Cn} \leq 0.035$ can guarantee convergent numerical solutions (Bai et al., 2017; Peng et al., 2021). Also, an empirical criterion $\text{Cn} \leq 4S$ (Yue et al., 2010), in which $S = l_d/R_0$ is the relative slip length, should be satisfied.

In summary, appropriate values for the lengths ϵ and l_d are typically on the nanometer scale for relevant physical problems. For a tube whose radius is on the order of 1 mm, this corresponds to dimensionless lengths Cn , $S = O(10^{-5})$. However, such severe length scales are difficult to resolve within PF-based numerical scheme, so to balance the computational loads and underlying physics, we instead chose $\text{Cn} = 0.01$ and $S = 0.004$ resulting in $l_s = 0.01R_0$. As indicated by Equation 1, the critical capillary number is proportional to $1/\ln l_s^{-1}$ and larger S would result in a larger critical capillary number. Nevertheless, the underlying physics and qualitative picture of geometrical impacts on interfacial dynamics should remain the same.

2.3.2. Viscosity Ratio and Capillary Number

We set the viscosity ratio $M = \mu_l/\mu_g$ to a fixed value of $M = 50$, to represent air entering a tube of water. The capillary number measures the strength of viscous stresses relative to surface tension. We use the maximum average velocity $U_0 = Q_{\text{in}}/(\pi R_0^2)$ to define the global capillary number $\text{Ca} = U_0\mu_l/\sigma$, which characterizes the viscous bending effect throughout the displacement process. Importantly, unlike displacement in a straight tube where the radially averaged velocity \bar{U} remains constant ($\bar{U} = U_0$) due to the uniform tube radius, in the case of a gradient tube with radius changing along the z axis as $R = R_{\text{in}} + kz$, the radially averaged velocity varies according to $\bar{U}(z) = U_0(R_0/R)^2$. To better understand how the tube geometry impacts the interfacial dynamics, we introduce a local capillary number $\text{Ca}_z = \text{Ca}(R_0/R)^2$. We anticipate that interface stability will change locally with Ca_z .

2.4. Interfacial Stability

Previous analysis of two-phase flow in capillary tubes suggests that the interface shape is made up of a boundary region close to the tube wall where viscous and capillary forces compete, and an outer region close to the center of the tube where surface tension dominates (Gao et al., 2019; Zhao et al., 2018). In the boundary layer, viscous forces bend the contact line, changing its slope from the local microscopic contact angle θ_{eq} to an apparent bulk contact angle θ_{app} . The bulk shape is then a spherical cap whose radius of curvature is set directly by θ_{app} . The consequent θ_{app} for a given θ_{eq} depends on the capillary number Ca , but is fixed throughout an experiment in a tube with straight walls (Gao et al., 2019; Zhao et al., 2018). Gao et al. (2019) predicted that the system becomes unstable at the critical value of Ca for which the apparent contact angle reaches $\theta_{\text{app}} = 0$. Beyond this value, a spherical cap cannot be maintained and the interface stretches out, leading to liquid entrainment and eventually capillary pinch-off (Zhao et al., 2018). This instability has been predicted theoretically from predictions of θ_{app} , and was observed experimentally by measuring the speeds of the contact line and cap front: in the stable regime, the contact line and cap front travel at the same speed, but in the unstable regime the cap front accelerates away from the contact line. An abrupt drop in the contact line velocity is typically observed, driving entrainment (Gao et al., 2019; Zhao et al., 2018).

In this work, we investigate two-phase flow in tubes with gradient walls instead of straight walls. For a fixed inlet velocity, conservation of mass tells us that the flow speed should increase as the tube narrows or decrease as the tube widens, leading to local changes in the balance between viscous stresses and capillary forces in the wall boundary region. We can interpret this as a change in the effective capillary number, which leads to a local change in θ_{app} . In other words, we expect to observe a moving front with a spherical cap whose curvature is evolving, until the flow reaches a speed (i.e., capillary number) beyond which a spherical cap cannot be maintained. It is not clear a priori whether this will correspond exactly to the threshold where the theoretical prediction of θ_{app} reaches zero, but we can investigate in our simulations by tracking the relative velocity jump

$$\Delta u = \frac{U_{tip} - U_{cl}}{U_0}, \quad (8)$$

where U_{tip} is the speed of the outermost tip of the moving front, U_{cl} is the speed of the moving contact line, and U_0 is the speed at the inlet. In our numerical simulations, we set a threshold of 1% for Δu , beyond which we regard the system to have transitioned from an evolving spherical cap to entrainment. In some scenarios, the interface will travel the full length of the tube with a shape that is an evolving spherical cap - we refer to this as a “stable” scenario, and to scenarios where entrainment occurs as “unstable”.

3. Results and Discussion

3.1. Simulation Results

We investigate the transition of the system outlined in Section 2 from stable to unstable displacement by performing a parameter sweep through Ca , θ_{eq} and slope angle α . Figure 2 illustrates the interface shape just before the tip of the interfacial front reaches the outlet for different capillary numbers and equilibrium contact angles. As Ca is increased (by increasing the inlet velocity), the displacement mode transitions from stable to unstable for each case, with the phase boundary marked by red solid lines in Figure 2a. In the stable mode, the meniscus takes the form of an evolving spherical cap throughout the simulation. In the unstable mode, interfacial instability occurs at a certain position, resulting in finger-shaped meniscus and entrainment of a liquid film on the tube wall. This mode transition is highly dependent on the wettability (θ_{eq}). For the expanding tube, shown in Figure 2b, for $\theta_{eq} = 30^\circ$, the mode transition occurs at around $Ca = 0.018$, while for $\theta_{eq} = 45^\circ$, it occurs at around $Ca = 0.045$. In other words, a smaller θ_{eq} , indicating a more hydrophilic tube wall, results in a more significant viscous bending effect and makes the instability more likely to occur.

In the following, we provide more insights into how the interface evolves in the contracting and expanding geometries, and especially focus on its transition from a stable to unstable state, and the reverse. Specifically, we track the change of moving speed of the interface at the symmetry axis (U_{tip}) and the contact line (U_{cl}), non-dimensionalized as Ca_{tip} and Ca_{cl} correspondingly. For the stable regime, we also measure the apparent contact angle θ_{app} by fitting a spherical cap to the interface shape at each time step. Specifically, the interfacial profile under the axisymmetric condition is assumed to be an arc whose center and radius are determined by fitting the extracted interface position using the equation of circles, and θ_{app} is calculated at the contact point.

3.1.1. Drainage in Contracting Tubes

Simulation results for a contracting tub ($k < 0$) are illustrated in Figure 3. In this scenario, the average axial velocity and hence the local capillary number Ca_z increases as the gas-liquid interface moves forward along the z axis. As Ca_z increases, the curvature of the interface must also increase so that surface tension balances viscous stresses. This leads to a decrease in the apparent contact angle θ_{app} , as illustrated over three frames in Figure 3a. As long as the viscous bending effect can be balanced by the capillary force, the interface shape remains close to a spherical cap - although its radius of curvature and hence the apparent contact angle θ_{app} decrease continuously as shown in 3(c). Furthermore, the speed of the interface at the symmetry axis (U_{tip}) and the contact line (U_{cl}) both increase but are almost identical at all times in this simulation, as shown in Figure 3b.

The system transitions to an unstable state once Ca_z exceeds a critical value Ca_{crit} , as illustrated in Figure 3d. In the early (stable) part of the simulation, the apparent tip and contact line speeds increase simultaneously (Figure 3e) and the apparent contact angle θ_{app} decreases smoothly. Instability occurs when θ_{app} reaches zero and the tip and contact line speeds diverge. A thin film is entrained on the tube wall, which hinders the movement of

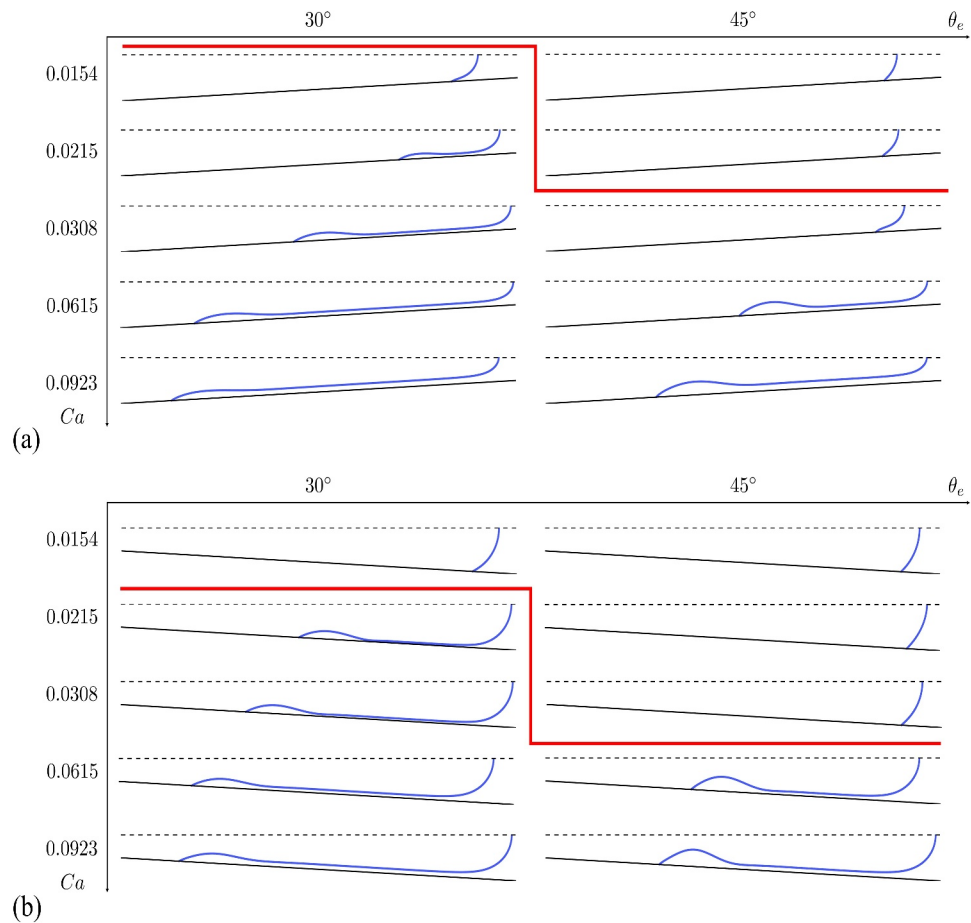


Figure 2. Final interfacial profiles before the interfacial tip touches the outlet under various θ_{eq} and Ca for the contracting tube (a) and the expanding tube (b). The red lines separate cases into stable and unstable ones.

the contact line, as shown in 3(d). As a result, U_{cl} sharply declines while U_{tip} continues to increase after instability, as illustrated in Figure 3e.

3.1.2. Drainage in Expanding Tubes

The drainage process in an expanding tube is more complex than in a contracting tube. Due to the decrease in local capillary number Ca_z along the tube axis, the viscous bending effect is weakened, and an initially unstable drainage process may become stable after a transition period if Ca is small enough. Figure 4a illustrates an example with $Ca = 0.0154$ and $\theta_{eq} = 30^\circ$. At the early stage, a finger-shaped interface is generated by the significant difference between U_{tip} and U_{cl} , as shown in Figure 4b. However, U_{tip} decreases more rapidly U_{cl} , and there is a brief “transition” period in which $U_{cl} > U_{tip}$ and the contact line can “catch up” with the tip to form a spherical cap shape, beyond which the velocities converge. Simultaneously, as the viscous effect decreases, θ_{app} increases from zero, corresponding to the beginning of the transition period as shown in Figure 4c.

For larger values of Ca , the viscous force exerts significant bending at the early time, and an entrained film forms quickly, as illustrated in Figure 4d for $Ca = 0.0215$. In this scenario, U_{tip} remains higher than U_{cl} throughout the drainage process, and interfacial stability cannot be attained within the tube length considered here.

3.2. Summary of Observations

The behavior of an advancing interface in a capillary tube is determined by competition between viscous bending and capillary resistance. Surface tension acts to minimize the interfacial area and maintain a minimal gradient in interfacial velocity across the interface. For a contracting tube, the viscous bending effect increases in time due to

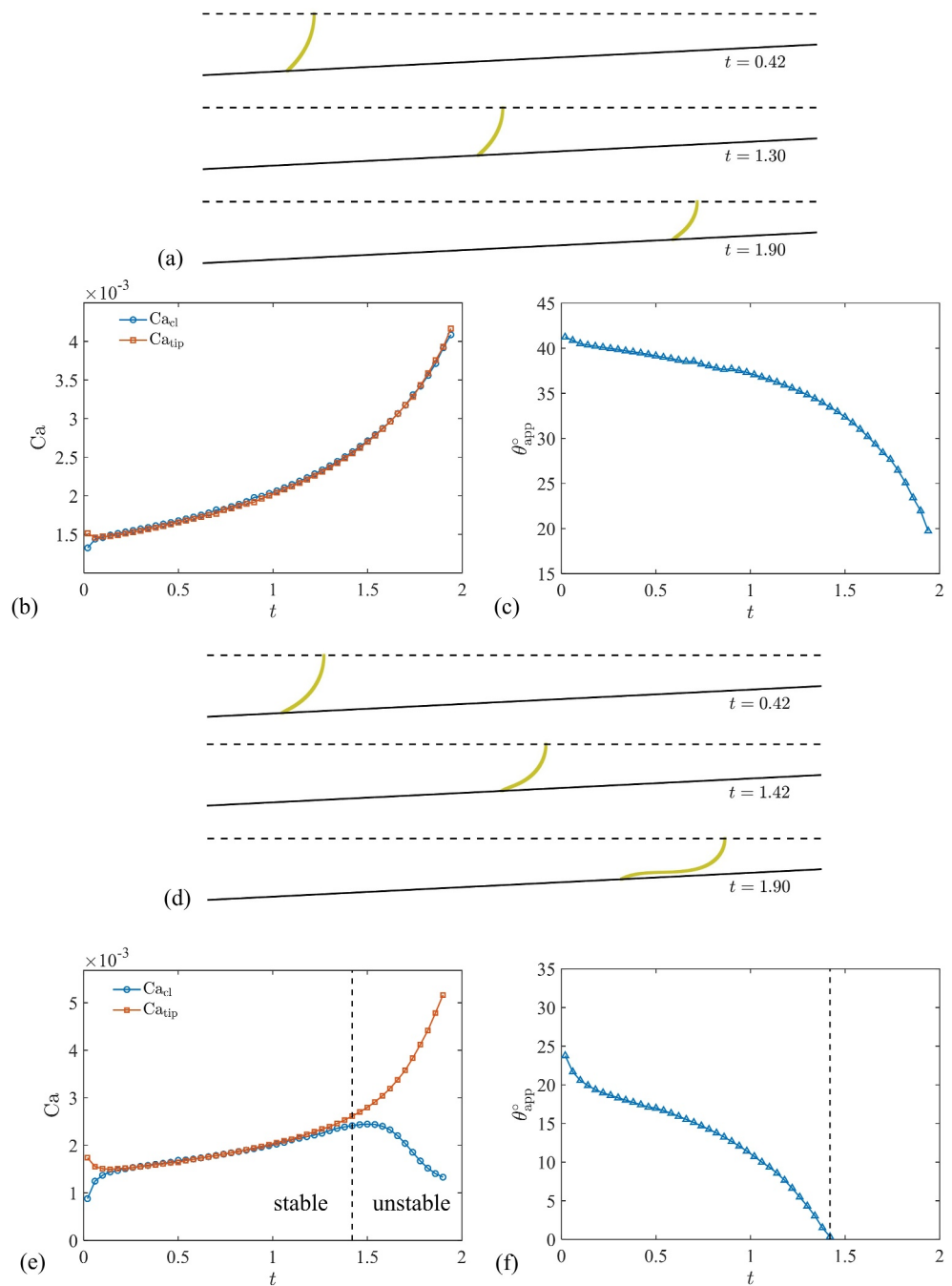


Figure 3. Film drainage in contracting tubes with $Ca = 0.0215$. Interfacial profiles, the corresponding scaled velocity at the meniscus tip (Ca_{tip}) and the contact line (Ca_{cl}), and the measured apparent contact angle (θ_{app}) are shown for $\theta_{eq} = 45^\circ$ (a, b, c) and $\theta_{eq} = 30^\circ$ (d, e, f). The dashed line in (e), (f) marks the position at which $\Delta u = 1\%$ is attained.

an increase in Ca_z . If an interfacial instability occurs at any point during the simulation, it will continue to develop as Ca_z increases further. For an expanding tube, the viscous bending effect decreases and the capillary effect may dominate the flow eventually. Therefore, even when $\Delta u \geq 1\%$ and the interface is unstable at the start of the instability, interfacial instability can be suppressed as long as significant liquid entrainment does not occur.

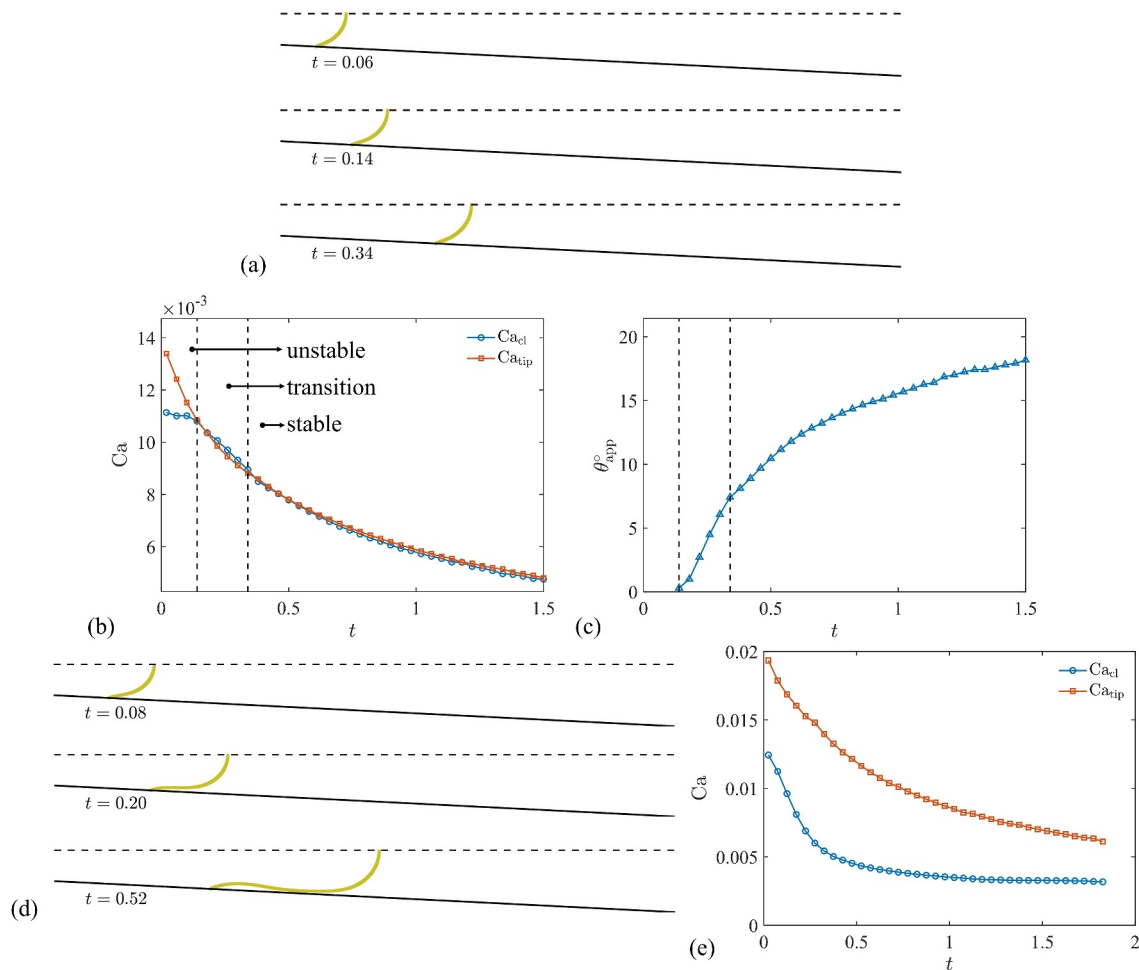


Figure 4. Evolution of interfacial profiles in the expanding tube, the corresponding scaled velocity at the meniscus tip (Ca_{tip}) and the contact line (Ca_{cl}), and the measured apparent contact angle (θ_{app}) for $\theta_{eq} = 30^\circ$ under $Ca = 0.0154$ (a, b, c) and $Ca = 0.0215$ (d), (e). The dashed lines mark the position of $\Delta u = 1\%$.

3.3. Critical Capillary Number

The simulation results reported above (and results for cylindrical tubes in the literature) suggest that there exists a critical capillary number Ca_{crit} beyond which the interface becomes unstable during a drainage process. To investigate this further, we use the theoretical model of Gao et al. (2019), who predicted the critical capillary number of a cylindrical tube. Adapting their methodology to the case of a gradient tube yields a methodology for predicting the apparent contact angle and dimensionless contact-line-to-tip distance $\Delta Z_{cl}/R$; details are given in Appendix B.

For each of the simulations presented above, we compare the instantaneous capillary number Ca_z with the theoretical threshold value Ca_{crit} which is determined based from (B4) and (B5) (see Figures 5a and 5b). The comparison can be used to rationalize some of the observations of Figure 2: for the cases of $Ca = 0.0154$ and 0.0215 when $\theta_{eq} = 45^\circ$, Ca_z is lower than Ca_{crit} along the full length of both expanding and contracting tubes, and correspondingly a fully stable drainage process is observed. Conversely, for the case of $Ca = 0.0923$, Ca_z is above Ca_{crit} along the full length of both expanding and contracting tubes, and film entrainment is observed. For intermediate capillary numbers in contracting tubes, Ca_z crosses the threshold value during the drainage process and the interface becomes unstable. In particular, for a contracting tube, the corresponding critical position z_{cr} , at which instability starts to develop, can be predicted accordingly using the intersection point of Ca_z and Ca_{crit} . The prediction is validated by comparing with the numerical results, as shown in Figure 5c.

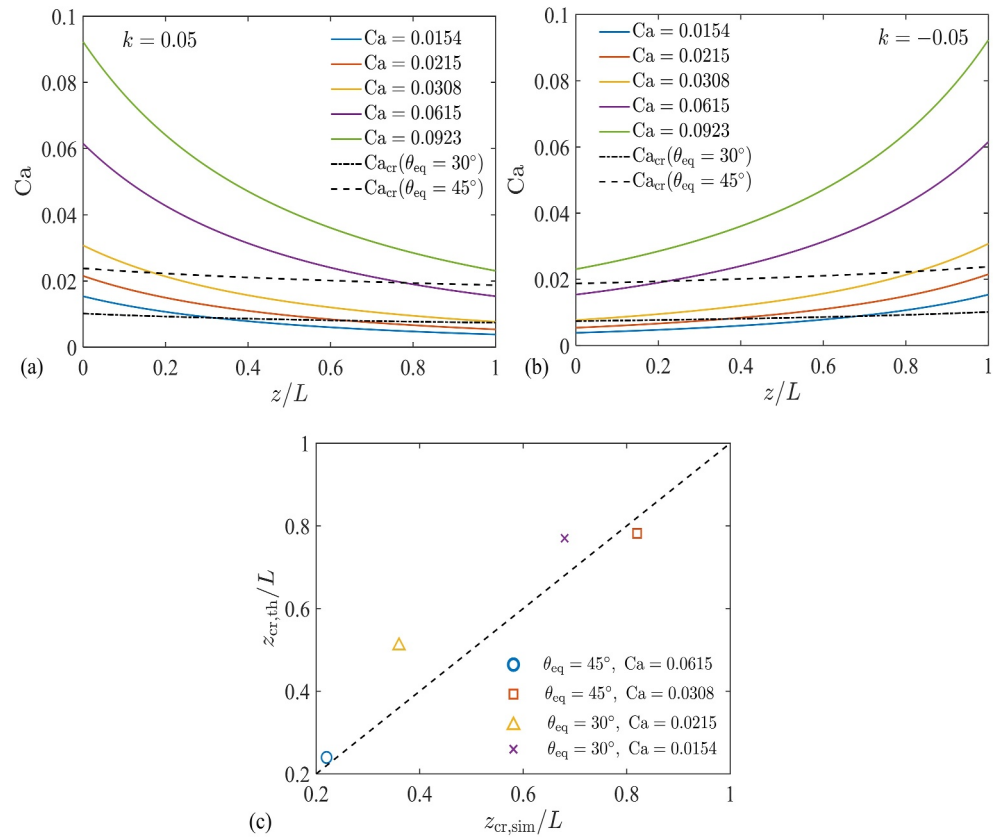


Figure 5. The local capillary number Ca_z along the tube compared with critical capillary number Ca_{crit} of $\theta_{eq} = 30^\circ$ and 45° for (a) $k = 0.05$ and (b) $k = -0.05$. (c) The comparison on the start position z_{cr} of instability between theoretical and numerical results, named $z_{cr,th}$ and $z_{cr,sim}$ separately.

Since the theoretical model is derived based on the quasi-steady assumption, it cannot predict interface dynamics after instability. In particular, the model cannot reliably predict the transition to a stable interface observed in expanding tubes in Figure 4. For the case of $Ca = 0.154$ and $\theta_{eq} = 30^\circ$, Ca_z is initially above Ca_{crit} and then decreases below it, and the system does indeed transition from unstable to stable. However, for the case with $Ca = 0.215$ this stabilization is not observed, even though Ca_z does cross the stability threshold. A complete theoretical analysis of the transition to stability is beyond the scope of the current work.

Besides the critical position z_{cr} , We conclude our theoretical analysis by comparing the tip-to-contact line length $\Delta Z_{cl}/R$ for a stable interface to the value observed in simulations. If we assume the interface shape is a spherical cap, then we can approximate (see Appendix B for details)

$$\frac{\Delta Z_{cl}}{R} = \frac{1 - \sin(\theta_{app} - \alpha)}{\cos(\theta_{app} - \alpha)}. \quad (9)$$

Figure 6 illustrates the comparison between the ΔZ_{cl} values extracted from the simulated interfaces and those predicted by the theoretical model. For $\theta_{eq} = 30^\circ$, the theoretical prediction closely matches the simulation results. However, when $\theta_{eq} = 45^\circ$, a significant mismatch is observed especially in the low- Ca_z region, as shown in Figure 6b. This discrepancy is likely due to the small- θ_{eq} and steady-interface assumptions employed in the theory. In a uniform tube, where the shape of the interface remains unchanged under a small Ca during the displacement, the theoretical prediction agrees well with simulations (Gao et al., 2019) and experiments (Zhao et al., 2018). However, in a gradient tube, the interface evolves continuously with the ongoing displacement, especially in a contracting tube where the movement of the interface is accelerated, and the dynamic effects may not be negligible.

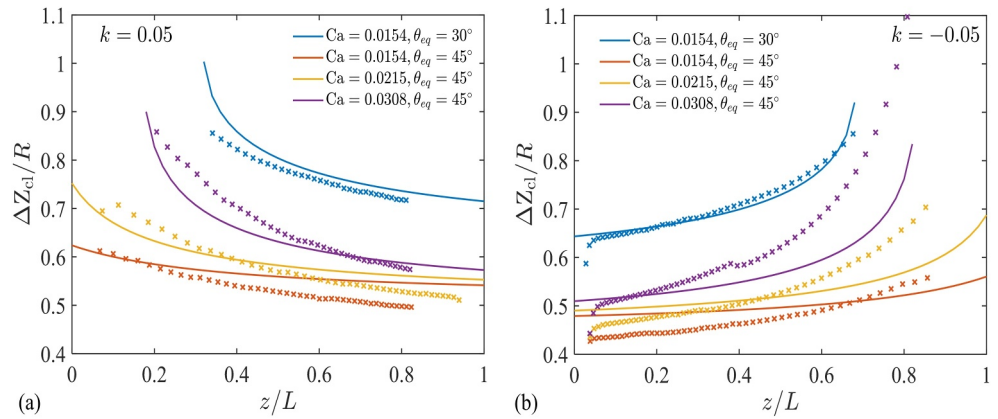


Figure 6. The evolution of ΔZ_{cl} along the tube for various Ca , k and θ_{eq} . The symbols (\times) represent the simulation results and the curves correspond to the theoretical predictions.

In summary, we present a theoretical model that is built on Eggers' approach, which involves matching the local contact line solution with the far-field meniscus to determine the stable interface shape and critical capillary number. Our model effectively describes the drainage process in a contracting tube. However, when applied to an expanding tube, our theoretical framework only offers a conservative prediction for displacement stability. Specifically, a fully stable interface is achieved when $Ca < Ca_{crit}$.

4. Post-Instability Dynamics

When the local capillary number, Ca_z , exceeds a critical value, Ca_{crit} , the meniscus is unable to maintain a spherical cap and becomes unstable. If this instability further develops, it can result in the gas phase penetrating the liquid phase to form a gas finger, while a thin film is entrained on the wall. Between the contact line and the entrained film, a dewetting rim forms. Consequently, there appear three representative regions, that is, the rim, connection and finger regions whose interfacial curvatures are significantly different, as shown in Figure 7a. As the viscosity of the gas phase can be neglected, the pressure in the gas phase P_g is uniformly distributed. According to the Young-Laplace equation, the corresponding pressures P_r , P_c and P_f can be estimated as.

$$P_r = P_g - \sigma \left(\frac{1}{r_{r,o}} - \frac{1}{r_{r,i}} \right), \tag{10}$$

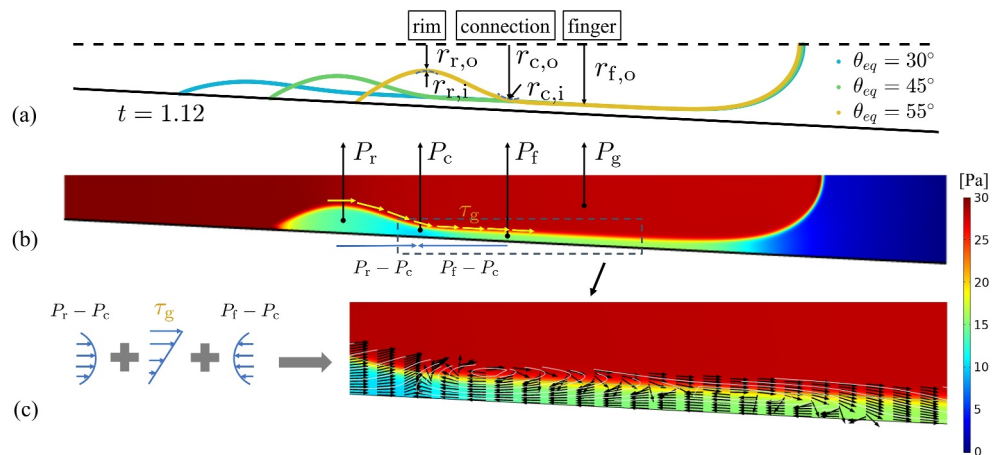


Figure 7. (a) Representative shapes of dewetting rims with $\theta_{eq} = 30^\circ, 45^\circ$ and 55° for $Ca = 0.0923$ and $k = 0.05$. (b) The corresponding contour plot of the pressure field for $\theta_{eq} = 45^\circ$ and (c) its zoom-in plot indicating the recirculation zone, where the white lines represent the stream lines and black arrows indicate the local velocity directions.

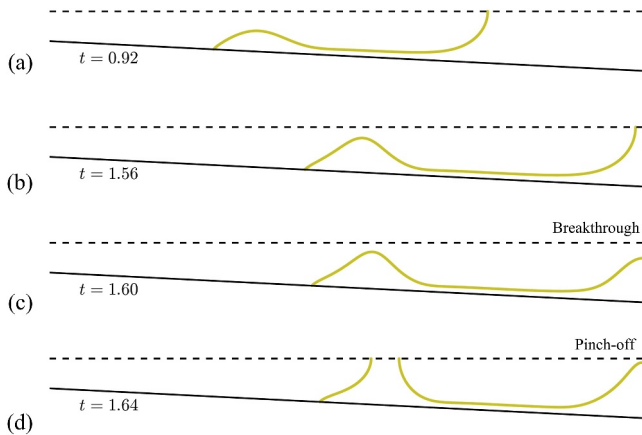


Figure 8. Process of a bubble pinch-off for $\theta_{eq} = 55^\circ$, $k = 0.05$ and $Ca = 0.0923$. The Ca_z is over Ca_{crit} , see Figure 5(a).

$$P_c = P_g - \sigma \left(\frac{1}{r_{c,o}} + \frac{1}{r_{c,i}} \right), \quad \text{and} \quad (11)$$

$$P_f = P_g - \frac{\sigma}{r_{f,o}}, \quad (12)$$

Where $1/r$ is the curvature of the interface, and the subscripts o and i represent the axial and hoop directions respectively. As conceptualized in Figure 7a, $P_c < P_f$ and $P_c < P_f$. Thus, this capillary effect leads to a low-pressure zone at the connection. Liquid is sucked along the tube toward this low-pressure zone from both sides, and must then move radially inwards where the flows from the two directions meet. The injected gas then applies a shear stress on the top of liquid film driving the liquid film flowing toward the outlet, leading to the development of a recirculation zone, as shown in Figures 7b and 7c. If the effect of $P_f - P_c$ surpasses the other two, the net flow of liquid would be from the outside to the rim region, causing the liquid to collect at the rim and allowing it to grow higher until gas bubble pinch-off occurs, that is, the so-called Taylor bubble forms (Taylor, 1961).

The shape of the rim mainly depends on the equilibrium contact angle, θ_{eq} . The larger θ_{eq} is, the higher the rim becomes, as shown in Figure 7a, resulting in lower pressure at the rim. Therefore, pinch-off is more likely to occur with a larger θ_{eq} . Figure 8 demonstrates the formation of a Taylor bubble for $\theta_{eq} = 55^\circ$, $k = 0.05$ and $Ca = 0.0923$. Notably, unlike in a uniform tube, where a train of traveling bubbles can form, in an expanding tube, the pinch-off process stops once the newly formed meniscus is located within a stable regime where $Ca_z < Ca_{crit}$. Furthermore, for a contracting tube, since the viscous effect is enhancing, we could expect an extremely long bubble would appear and even the pinch-off would not occur. However, the related quantitative picture remains to be explored.

5. Conclusions

In this study, we investigate the dynamics of the interface between a gas and a liquid when gas is used to displace a wetting liquid in a gradient capillary tube. Our focus is on understanding the impact of tube geometry on the stability of the liquid-gas interface. The simulations reveal that the interface remains stable as long as $Ca_z < Ca_{crit}$. Once Ca_z exceeds Ca_{crit} , for a contracting tube, the interface becomes unstable and the instability continuously develops. However, for an expanding tube, the instability is likely to be suppressed afterward, that is, a stability transition from an initially unstable meniscus to a final stable one can happen when Ca_z exceeds Ca_{crit} not too much. Our theoretical predictions rationalize the occurrence of fully stable and fully unstable spherical interfaces, as well as the dynamic transition from stable to unstable. However, a novel transition from instability back to stable interface propagation is observed in our simulations and warrants further investigations on the precise prediction of such a stabilizing effect. This work provides insights for estimating the mode and efficiency of fluid displacement in porous media with gradient pore structures. Since porous media can be regarded as a bundle of connected capillary tubes, the developed theoretical tools and discovered rules could in principle be integrated into pore-network methods to achieve a larger-scale modeling.

We note that the scope of this work is currently limited to the gas-liquid displacement in the unfavorable-displacement regime ($M \gg 1$). Further studies on the neutral- ($M \approx 1$) and favorable-displacement regime ($M \ll 1$), as well as extending the theory to consider different viscosity ratios, hold practical value and are areas of potential future investigation.

Appendix A: Validation of the Numerical Scheme

In this appendix, we validate numerical scheme employed in the paper by applying it to the special case of a straight capillary tube, as an extreme case. In Figure A1, we compare the tip length $\Delta Z_{cl}/R$ to the theoretical solution reported in Gao et al. (2019) for a range of Ca values. Our numerical results are in good agreement with the theoretical prediction, suggesting that the numerical scheme can accurately resolve the capillary and viscous effects in the tube.

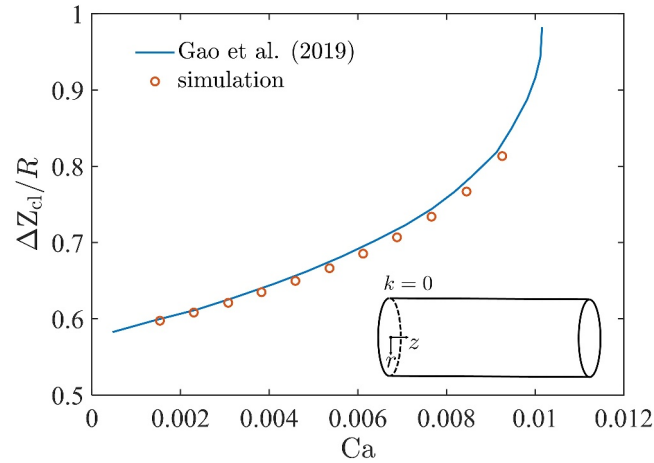


Figure A1. Comparison of representative interfacial profiles for $\theta_{eq} = 30^\circ$ and $S = 0.01$ between our simulation and a theoretical solution in Gao et al. (2019).

Appendix B: Critical Capillary Number Ca_{crit}

In this Appendix we adapt the derivation of Gao et al. (2019) of the critical capillary number Ca_{crit} beyond which instability occurs to the case of gradient tubes. The derivation requires matching between a smooth outer region where the interface is smooth, and a boundary layer near the wall where the interface slope adjusts rapidly to satisfy the contact angle. Notably, this approach relies on two fundamental assumptions: the “lubrication approximation” and the “spherical cap” in our situation. The former requires a small slope of the contact line, that is, small θ_{eq} , while the latter necessitates a small α .

First, we assume that the interface in the outer region is a spherical cap before the instability occurs. As shown in Figure B1, the local coordinate is based on the contact point with the x -axis aligned with the tube wall, and the outer solution of film thickness h_{out} satisfies the equation

$$(R + x \sin \alpha - h_{out} \cos \alpha)^2 + [R \tan(\theta_{app} - \alpha) + h_{out} \sin \alpha + x \cos \alpha]^2 = \frac{R^2}{\cos^2(\theta_{app} - \alpha)}. \quad (B1)$$

Multiplying out terms in (B1) yields a quadratic equation for h_{out} for a given apparent contact angle θ_{app} . We can determine the correct value of θ_{app} by matching with an inner solution h_{in} near the contact point, that is, for $x \ll 1$. Seeking an asymptotic expansion for h_{out} in powers of x yields

$$h_{out}(x) = x \tan \theta_{app} + \frac{\cos(\theta_{app} - \alpha)}{2R \cos^3 \theta_{app}} x^2 + O(x^3). \quad (B2)$$

The inner solution h_{in} , which is determined by the balance of the viscous force and the surface tension within the region $l_s \ll x \ll R$, is from Eggers' work (Eggers, 2005). In this problem, only the receding contact line is involved; additionally, the curvature of the tube wall can be ignored since $l_s \ll R$. Therefore, this problem is an analogy to pulling a flat plate from a liquid bath, and an asymptotic solution of h_{in} as a function of the reduced capillary number $\delta = 3 Ca / \theta_{eq}^3$ is

$$h_{in}(x) = \delta^{1/3} \left[\frac{\theta_{eq}^2 \kappa_y}{6 l_s} x^2 + \theta_{eq} b_y x + O(l_s) \right], \quad (B3)$$

where $\kappa_y = \left(\frac{2^{1/6} \beta}{\pi \text{Ai}(s_1)} \right)^2$, $b_y = -\frac{2^{2/3} \text{Ai}'(s_1)}{\text{Ai}(s_1)}$, $\beta^2 = \pi / 2^{2/3} e^{-1/(3\delta)} + O(\delta)$, and Ai is the Airy function. Notably, though the inner solution is derived based on the

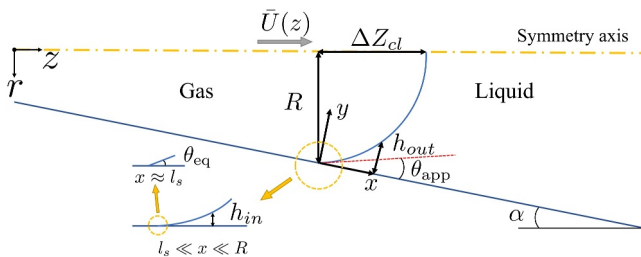


Figure B1. Schematic of the axisymmetric theoretical model in the global cylindrical coordinate r - z . Based on the contact point, a local coordinate is set to describe the film thickness at different length scales.

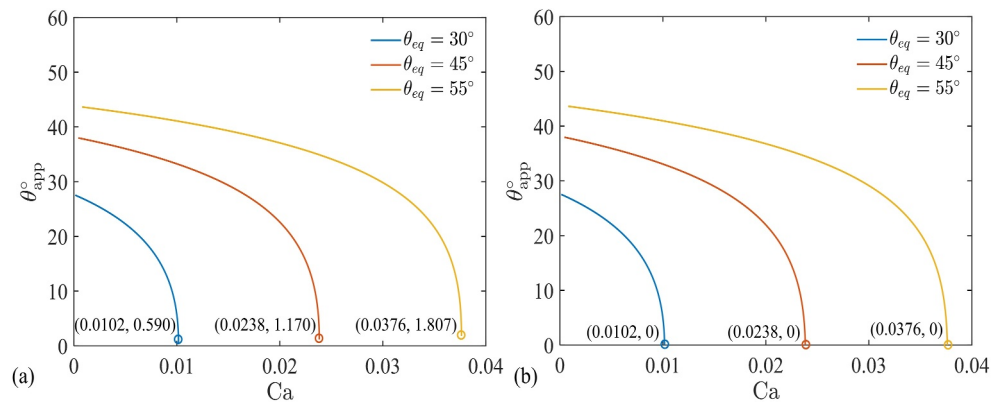


Figure B2. The variation of θ_{app} with Ca solved through (B4) and (B5) with $l_s = 0.01 R$ for (a) $k = 0.05$ and (b) $k = -0.05$. The critical capillary number Ca_{crit} and corresponding apparent contact angle $\theta_{app,crit}$ is labeled and marked with circles. The local capillary number Ca_s along the tube compared with critical capillary number Ca_{crit} for $\theta_{eq} = 30^\circ$ and 45° .

assumption that θ_{eq} is small, the comparison against numerical simulations indicates that it can be used for large contact angles, for example, $\theta_{eq} = 50^\circ$ (Gao et al., 2019). By comparing (B2) to (B3), two matching conditions are obtained.

$$\tan \theta_{app} = \delta^{1/3} \theta_{eq} b_y, \quad (B4)$$

$$\frac{\cos(\theta_{app} - \alpha)}{R \cos^3 \theta_{app}} = \frac{\delta^{1/3} \theta_{eq}^2 \kappa_y}{3l_s}. \quad (B5)$$

For a given Ca in a given tube (i.e., given θ_{eq} , α , R and l_s), the apparent contact angle θ_{app} and the auxiliary variable s_1 can be determined from the simultaneous equations (B4) and (B5). The critical capillary number Ca_{crit} can be determined by increasing Ca until (B4) and (B5) are not solvable. Figure B2(a) and B2(b) show the solution of θ_{app} versus Ca with various θ_{eq} and α , and the critical capillary number Ca_{crit} and the corresponding $\theta_{app,crit}$ are labeled for each case. In the case of a contracting tube ($k < 0$), Ca reaches the critical value when θ_{app} decreases to zero. Notably, for an expanding tube, $\theta_{app,crit}$ takes a small positive value but it is close to zero.

It is worth noting that as θ_{eq} and α increase, the applicability of our theoretical solution gradually diminishes. From the comparison against the simulations, we can confirm the applicability of our theoretical prediction within $k \in [-0.05, 0.05]$. However, determining the exact boundary of this limitation is out of the scope of this work.

Data Availability Statement

All numerical simulations in this work are implemented in COMSOL Multiphysics® v. 5.6 (www.comsol.com, COMSOL AB, Stockholm, Sweden).

References

- Al-Housseiny, T. T., Tsai, P. A., & Stone, H. A. (2012). Control of interfacial instabilities using flow geometry. *Nature Physics*, 8(10), 747–750. <https://doi.org/10.1038/nphys2396>
- Bai, F., He, X., Yang, X., Zhou, R., & Wang, C. (2017). Three dimensional phase-field investigation of droplet formation in microfluidic flow focusing devices with experimental validation. *International Journal of Multiphase Flow*, 93, 130–141. <https://doi.org/10.1016/j.ijmultiphaseflow.2017.04.008>
- Chen, Y.-F., Fang, S., Wu, D.-S., & Hu, R. (2017). Visualizing and quantifying the crossover from capillary fingering to viscous fingering in a rough fracture. *Water Resources Research*, 53(9), 7756–7772. <https://doi.org/10.1002/2017wr021051>
- Cox, R. (1986). The dynamics of the spreading of liquids on a solid surface. part 1. viscous flow. *Journal of Fluid Mechanics*, 168(1), 169–194. <https://doi.org/10.1017/s0022112086000332>
- Cuéllar-Franca, R. M., & Azapagic, A. (2015). Carbon capture, storage and utilisation technologies: A critical analysis and comparison of their life cycle environmental impacts. *Journal of CO2 Utilization*, 9, 82–102. <https://doi.org/10.1016/j.jcou.2014.12.001>
- Eggers, J. (2005). Existence of receding and advancing contact lines. *Physics of Fluids*, 17(8), 082106. <https://doi.org/10.1063/1.2009007>

Acknowledgments

This research was undertaken with the financial support of the Swedish Foundation for Strategic Research under SSF-FLL15-001. Access to the supercomputing resources of the PDC Center for High Performance Computing and National Supercomputer Centre (NSC) used for this work were provided by the National Academic Infrastructure for supercomputing in Sweden (NAISS).

- Gao, P., Liu, A., Feng, J. J., Ding, H., & Lu, X.-Y. (2019). Forced dewetting in a capillary tube. *Journal of Fluid Mechanics*, 859, 308–320. <https://doi.org/10.1017/jfm.2018.834>
- Holtzman, R., & Segre, E. (2015). Wettability stabilizes fluid invasion into porous media via nonlocal. *cooperative pore filling*. *Physical review letters*, 115(16), 164501. <https://doi.org/10.1103/physrevlett.115.164501>
- Jacqmin, D. (1999). Calculation of two-phase Navier–Stokes flows using phase-field modeling. *Journal of Computational Physics*, 155(1), 96–127. <https://doi.org/10.1006/jcph.1999.6332>
- Jacqmin, D. (2000). Contact-line dynamics of a diffuse fluid interface. *Journal of Fluid Mechanics*, 402, 57–88. <https://doi.org/10.1017/s0022112099006874>
- Khishvand, M., Alizadeh, A., Oraki Kohshour, I., Piri, M., & Prasad, R. (2017). In situ characterization of wettability alteration and displacement mechanisms governing recovery enhancement due to low-salinity waterflooding. *Water Resources Research*, 53(5), 4427–4443. <https://doi.org/10.1002/2016wr020191>
- Levaché, B., & Bartolo, D. (2014). Revisiting the saffman-taylor experiment: Imbibition patterns and liquid-entrainment transitions. *Physical Review Letters*, 113(4), 044501. <https://doi.org/10.1103/physrevlett.113.044501>
- Li, Y., Blois, G., Kazemifar, F., & Christensen, K. T. (2019). High-speed quantification of pore-scale multiphase flow of water and supercritical co2 in 2-d heterogeneous porous micromodels: Flow regimes and interface dynamics. *Water Resources Research*, 55(5), 3758–3779. <https://doi.org/10.1029/2018wr024635>
- Lu, N. B., Browne, C. A., Amchin, D. B., Nunes, J. K., & Datta, S. S. (2019). Controlling capillary fingering using pore size gradients in disordered media. *Physical Review Fluids*, 4(8), 084303. <https://doi.org/10.1103/physrevfluids.4.084303>
- Muhammed, N. S., Haq, B., Al Shehri, D., Al-Ahmed, A., Rahman, M. M., & Zaman, E. (2022). A review on underground hydrogen storage: Insight into geological sites, influencing factors and future outlook. *Energy Reports*, 8, 461–499. <https://doi.org/10.1016/j.egyrs.2021.12.002>
- Pahlavan, A. A., Stone, H. A., McKinley, G. H., & Juanes, R. (2019). Restoring universality to the pinch-off of a bubble. *Proceedings of the National Academy of Sciences*, 116(28), 13780–13784. <https://doi.org/10.1073/pnas.1819744116>
- Peng, X., Wang, X., Du, Z., & Zeng, F. (2021). Phase-field simulations of precursor film in microcapillary imbibition for liquid-liquid systems. *International Journal of Multiphase Flow*, 144, 103789. <https://doi.org/10.1016/j.ijmultiphaseflow.2021.103789>
- Primkulov, B. K., Pahlavan, A. A., Fu, X., Zhao, B., MacMinn, C. W., & Juanes, R. (2021). Wettability and lenormand’s diagram. *Journal of Fluid Mechanics*, 923, A34. <https://doi.org/10.1017/jfm.2021.579>
- Rabbani, H. S., Or, D., Liu, Y., Lai, C.-Y., Lu, N. B., Datta, S. S., et al. (2018). Suppressing viscous fingering in structured porous media. *Proceedings of the National Academy of Sciences*, 115(19), 4833–4838. <https://doi.org/10.1073/pnas.1800729115>
- Saffman, P. G., & Taylor, G. I. (1958). The penetration of a fluid into a porous medium or hele-shaw cell containing a more viscous liquid. *Proceedings of the Royal Society of London - Series A: Mathematical and Physical Sciences*, 245(1242), 312–329.
- Setu, S. A., Zacharoudiou, I., Davies, G. J., Bartolo, D., Moulinet, S., Louis, A. A., et al. (2013). Viscous fingering at ultralow interfacial tension. *Soft Matter*, 9(44), 10599–10605. <https://doi.org/10.1039/c3sm51571k>
- Suo, S., & Gan, Y. (2021). Tuning capillary flow in porous media with hierarchical structures. *Physics of Fluids*, 33(3), 034107. <https://doi.org/10.1063/5.0038634>
- Suo, S., Liu, M., & Gan, Y. (2020). Fingering patterns in hierarchical porous media. *Physical Review Fluids*, 5(3), 034301. <https://doi.org/10.1103/physrevfluids.5.034301>
- Taylor, G. (1961). Deposition of a viscous fluid on the wall of a tube. *Journal of Fluid Mechanics*, 10(2), 161–165. <https://doi.org/10.1017/s0022112061000159>
- Vincent-Dospital, T., Moura, M., Toussaint, R., & Måløy, K. J. (2022). Stable and unstable capillary fingering in porous media with a gradient in grain size. *Communications Physics*, 5(1), 306. <https://doi.org/10.1038/s42005-022-01072-1>
- Yang, Z., Méheust, Y., Neuweiler, I., Hu, R., Niemi, A., & Chen, Y.-F. (2019). Modeling immiscible two-phase flow in rough fractures from capillary to viscous fingering. *Water Resources Research*, 55(3), 2033–2056. <https://doi.org/10.1029/2018wr024045>
- Yuan, Q., Ma, Z., Wang, J., & Zhou, X. (2021). Influences of dead-end pores in porous media on viscous fingering instabilities and cleanup of naps in miscible displacements. *Water Resources Research*, 57(11), e2021WR030594. <https://doi.org/10.1029/2021wr030594>
- Yue, P., & Feng, J. (2011). Can diffuse-interface models quantitatively describe moving contact lines? *The European Physical Journal - Special Topics*, 197(1), 37–46. <https://doi.org/10.1140/epjst/e2011-01434-y>
- Yue, P., Feng, J. J., Liu, C., & Shen, J. (2004). A diffuse-interface method for simulating two-phase flows of complex fluids. *Journal of Fluid Mechanics*, 515, 293–317. <https://doi.org/10.1017/s0022112004000370>
- Yue, P., Zhou, C., & Feng, J. J. (2010). Sharp-interface limit of the cahn–hilliard model for moving contact lines. *Journal of Fluid Mechanics*, 645, 279–294. <https://doi.org/10.1017/s0022112009992679>
- Zhao, B., MacMinn, C. W., & Juanes, R. (2016). Wettability control on multiphase flow in patterned microfluidics. *Proceedings of the National Academy of Sciences*, 113(37), 10251–10256. <https://doi.org/10.1073/pnas.1603387113>
- Zhao, B., Pahlavan, A. A., Cueto-Felgueroso, L., & Juanes, R. (2018). Forced wetting transition and bubble pinch-off in a capillary tube. *Physical Review Letters*, 120(8), 084501. <https://doi.org/10.1103/physrevlett.120.084501>